The Orientation of the Local Interstellar Magnetic Field
M. Opher, *et al.*
Science **316**, 875 (2007);
DOI: 10.1126/science.1139480

of progressively more complex hydrocarbon molecules, from benzene to PAHs and ultimately to aerosol particles with ~260-nm radii. The existence of ~40,000-amu aerosols, formed by the growth of complex organic compounds in the upper atmosphere, appears to answer the long-unresolved question of the origin of tholin precursors found at Titan. The chain of molecular growth that we have identified in this study is similar to that first identified in the Miller-Urey experiments (*3*). We suspect that the ultimate destination of these large organic molecules and aerosols lies in the organic haze layers in Titan's stratosphere (*3*, *4*). However, depending on the dynamic effects of atmospheric and induced co-rotational electric fields on these particles, they might also escape Titan's atmosphere to become the source of PAHs observed to collect on the surfaces of Saturn's icy moons (*34*, *35*).

References and Notes

1. R. V. Yelle *et al.*, *Icarus* **72**, 468 (2006).
2. Y. L. Yung, M. Allen, J. P. Pinto, *Astrophys. J. Suppl. Ser.* **55**, 465 (1984).
3. C. Sagan, B. N. Khare, *Nature* **277**, 102 (1979).
4. C. P. McKay *et al.*, *Planet. Space Sci.* **49**, 79 (2001).
5. A. Coustenis *et al.*, *Icarus*, in press; available online at http://dx.doi.org/10.1016/j.icarus.2006.12.022.
6. H. Richter, J. B. Howard, *Prog. Energy Combust. Sci.* **26**, 565 (2000).
7. H. F. Calcote, D. G. Keil, *Pure Appl. Chem.* **62**, 815 (1990).
8. M. Frenklach, *Phys. Chem. Chem. Phys.* **4**, 2028 (2002).
9. A. A. Pavlov, M. T. Hurtgen, J. F. Kasting, M. A. Arthur, *Geology* **31**, 87 (2003).
10. J. H. Waite Jr. *et al.*, *Science* **308**, 982 (2005).
11. D. T. Young *et al.*, *Space Sci. Rev.* **114**, 1 (2004).
12. A. J. Coates *et al.*, *Eos Trans. Am. Geophys. Union* **87** (fall meeting suppl.), 52, abstract P21B-06 (2006).
13. E. H. Wilson, S. K. Atreya, A. Coustenis, *J. Geophys. Res. (Planets)* **108**, 5014 (2003).
14. V. De La Haye, thesis, University of Michigan, Ann Arbor, MI (2005).
15. T. E. Cravens *et al.*, *Geophys. Res. Lett.* **32**, L12108 (2005).
16. V. Vuitton, R. V. Yelle, V. G. Anicich, *Astrophys. J.* **647**, L175 (2006).
17. D. K. Bohme, *Chem. Rev.* **92**, 1487 (1992).
18. All minor neutral constituents (with the exception of methane) show molecular diffusive scale heights at our lowest altitude on T16, most notably the inert species ^{40}Ar. We can use the mixing ratio of ^{40}Ar measured in the lower atmosphere by the Huygens Gas Chromatograph Mass Spectrometer [4.32×10^{-5} (*33*)] and the ^{40}Ar mixing ratio measured by the INMS on T16 at 975 km of $1.46 \times 10^{-5} \pm 0.14 \times 10^{-5}$ to infer that the homopause or turbulent mixing boundary lies ~110 km below our observation point (865 ± 25 km), where the altitude uncertainty represents uncertainties in the atmospheric temperature profile and the mixing ratio of ^{40}Ar. The lack of compliance of methane with a molecular diffusive scale height has been suggested as due to outflow (*1*, *2*).
19. National Institute of Standards and Technology (NIST) Chemical Kinetics Database (www.kinetics.nist.gov/kinetics/index.jsp).
20. I. V. Tokmakov *et al.*, *J. Phys. Chem. A* **103**, 3636 (1999).
21. J. Crovisier, *J. Geophys. Res.* **99**, 3777 (1994).
22. J. I. Moses *et al.*, *J. Geophys. Res.* **110**, e08001 (2005).
23. A. Yokoyama *et al.*, *J. Chem. Phys.* **92**, 4222 (1990).
24. K. Shindo, S. Lipsky, *J. Chem. Phys.* **45**, 2292 (1966).
25. N. Nakashima, Y. Keitaro, *J. Chem. Phys.* **79**, 2727 (1983).
26. We calculated vapor pressure (*P*) values using the Antoine equation [$\log P = A - B/(T + C)$] and the parameters *A*, *B*, and *C* using experimental data in a specific temperature (*T*) range. The extrapolation of these data by means of the Antoine equation to lower temperatures has been verified with the use of benzene and methane data. We performed a verification by producing a test case where the Antoine equation fit was produced using only the high-temperature values, which we then compared with the experimental low-temperature data. Our test case shows a maximum uncertainty of one decade at the extreme low temperatures (less than 100 K) and, at 130 K, the extrapolated data differ by a factor of five. The parameters *A*, *B*, and *C* are obtained from (*36*).
27. A. J. Friedson, A.-S. Wong, Y. L. Yung, *Icarus* **158**, 389 (2002).
28. T. Moustefaoui *et al.*, *Faraday Discuss. Chem. Soc.* **109**, 71 (1998).
29. X. Zhang *et al.*, *Chem. Commun.* **2006**, 758 (2006).
30. C. K. Goetz, *Rev. Geophys.* **27**, 271 (1989).
31. M. G. Kivelson, C. T. Russell, Eds. *Introduction to Space Physics* (Cambridge Univ. Press, Cambridge, 1995).
32. M.-C. Liang, Y. L. Yung, D. E. Shemansky, paper presented at the 38th Annual Meeting of the Division of Planetary Sciences, American Astronomical Society, Pasadena, CA, 8 to 13 October 2006.
33. H. B. Niemann *et al.*, *Nature* **438**, 779 (2005).
34. D. P. Cruickshank *et al.*, *Icarus*, in press.
35. R. N. Clark *et al.*, *EOS Trans. Am. Geophys. Union*, **87** (fall meeting suppl.), abstract P32A-03 (2006).
36. P. J. Linstrom, W. G. Mallard, Eds. *The National Institute of Standards and Technology Chemistry WebBook* (NIST Standard Reference Database Number 69, June 2005 release); (http://webbook.nist.gov/chemistry/).
37. J. L. McLain, V. Poterya, C. D. Molek, L. M. Babcock, N. G. Adams, *J. Phys. Chem. A* **108**, 6704 (2004).
38. V. G. Anicich, "An index of the literature for bi-molecular gas-phase-cation-molecule reaction kinetics" (NASA Jet Propulsion Laboratory, JPL Publication 03-19, Pasadena, CA, 2003).
39. V. G. Anicich, M. McEwan, *Planet. Space Sci.* **45**, 897 (1997).
40. V. G. Anicich, P. F. Wilson, M. J. McEwan, *J. Am. Soc. Mass Spectrom.* **17**, 544 (2006).

41. We thank NASA for its continuing support of operations and data analysis from the Cassini mission and A.J.C. thanks the Science and Technology Facilities Council for support of ELS. The INMS and CAPS teams acknowledge support from NASA and the Jet Propulsion Laboratory (SWRI subcontract numbers 1283095 and 1243218, respectively), as well as the support of their respective science and operations teams. J.H.W. acknowledges numerous helpful discussions with G. R. Gladstone, and A.J.C. acknowledges help with the data analysis from G. R. Lewis.

9 January 2007; accepted 26 March 2007
10.1126/science.1139727

The Orientation of the Local Interstellar Magnetic Field

M. Opher,[1]* E. C. Stone,[2] T. I. Gombosi[3]

The orientation of the local interstellar magnetic field introduces asymmetries in the heliosphere that affect the location of heliospheric radio emissions and the streaming direction of ions from the termination shock of the solar wind. We combined observations of radio emissions and energetic particle streaming with extensive three-dimensional magnetohydrodynamic computer simulations of magnetic field draping over the heliopause to show that the plane of the local interstellar field is ~60° to 90° from the galactic plane. This finding suggests that the field orientation in the Local Interstellar Cloud differs from that of a larger-scale interstellar magnetic field thought to parallel the galactic plane.

The heliosphere created by the supersonic solar wind is compressed by the motion of the Sun relative to the local interstellar medium, producing a comet-like shape with an extended tail. The solar wind abruptly slows, forming a termination shock as it approaches contact with the interstellar medium at the heliopause. Beyond the heliopause, the interstellar wind contains mainly hydrogen and helium, both as neutral atoms and as ions that carry the frozen-in interstellar magnetic field.

Recent Voyager observations of ions streaming from the termination shock (*1*, *2*) have led to the suggestion that north-south and east-west asymmetries of the heliosphere are induced by the interstellar magnetic field (*3*). However, the inferred field direction from the model of (*3*) was parallel to the hydrogen deflection plane (HDP) rather than the galactic plane (GAL). On the basis of the polarization of light from nearby stars, Frisch (*4*, *5*) suggested that the galactic magnetic field is parallel to the GAL. However, the direction of the galactic magnetic field is deduced from measurements averaged over a much larger distance (light-years). A direction parallel to the HDP was suggested by Lallement *et al*. (*6*) for the local interstellar field, on the basis of solar Lyman-α radiation that is resonantly backscattered by interstellar hydrogen atoms. The HDP is tilted from the ecliptic plane by 60° and differs from the GAL by 60°. We used Voyager 1 and 2 observations in conjunction with a magnetohydrodynamic model to discriminate between these two planes and to constrain the orientation of the local interstellar magnetic field.

[1]Department of Physics and Astronomy, George Mason University, 4400 University Drive, Fairfax, VA 22030, USA. [2]California Institute of Technology, Pasadena, CA 91125, USA. [3]Center for Space Environment Modeling, University of Michigan, Ann Arbor, MI 48109, USA.

*To whom correspondence should be addressed. E-mail: mopher@physics.gmu.edu

In the past 20 years, Voyager 1 (V1) and 2 (V2) have been detecting radio emissions in the outer heliosphere at frequencies from 2 to 3 kHz (*7*–*9*). The radio emissions were detected each solar cycle: first in 1983–1984 during solar cycle 21 (*7*), second in 1992–1994 during solar cycle 22 (*8*), and most recently during solar cycle 23 (*9*). The currently accepted scenario is that the radio emissions are generated when a strong interplanetary shock produced by a period of intense solar activity reaches the vicinity of the heliopause and moves into the interstellar plasma beyond (*9*, *10*). Radio direction-finding measurements from V1 and V2 have been used to determine the positions near the heliopause at which the radio emissions are generated (*11*) (Fig. 1). The sources lie along a line that passes near the nose of the heliosphere that roughly parallels the GAL. The GAL is 120° from the ecliptic plane (*12*). Because the galactic magnetic field is oriented nearly parallel to the GAL, Kurth and Gurnett (*11*) suggested that the local interstellar magnetic field (in the local neighborhood of the Sun) was also parallel to the GAL.

However, Gurnett *et al*. (*13*) recently pointed out that at Earth's bow shock and interplanetary shocks, the radio emission occurs where the magnetic field lines are tangential to the shock surface, and they suggested that heliospheric radio emissions occur where the local interstellar magnetic field is tangential to the surface of the shock that excites the plasma (or $\mathbf{B}\cdot\mathbf{n} = 0$, where $\mathbf{B}$ is the magnetic field and $\mathbf{n}$ is the shock normal). They concluded that the condition $\mathbf{B}\cdot\mathbf{n} = 0$, combined with the source location observed by the two Voyager spacecraft, implies that the local interstellar magnetic field is perpendicular to the GAL. This direction differs from the earlier suggestion (*9*) and is within 16° of the HDP.

The interstellar magnetic field is frozen into interstellar plasma that is deflected around the heliopause, causing the field to drape over the heliopause. As a result, the region where $\mathbf{B}\cdot\mathbf{n} = 0$ will depend on the shape of the heliopause, which is distorted by pressure of the local interstellar magnetic field. For intensities around a few microgauss, the ambient interstellar magnetic pressure is comparable to the gas pressure, with the magnetic pressure increasing in those regions where the interstellar flow decreases as it approaches the heliopause. We investigated how the proposed location of the radio sources (where $\mathbf{B}\cdot\mathbf{n} = 0$ on the surface of the heliopause) varies with the orientation and strength of the local interstellar magnetic field.

We considered several directions of the interstellar magnetic field—the HDP, the GAL, and the plane perpendicular to the radio source plane (*13*) (PPG)—with different inclination angles α (the angle between the interstellar magnetic field and interstellar wind velocity). In the model coordinate system, where β is the angle between the interstellar magnetic field and the solar equator, the HDP corresponds to $\beta = 60°$, the GAL to $\beta = 120°$, and the PPG to $\beta = 44°$ (*12*). Assuming a spherical interplanetary shock,

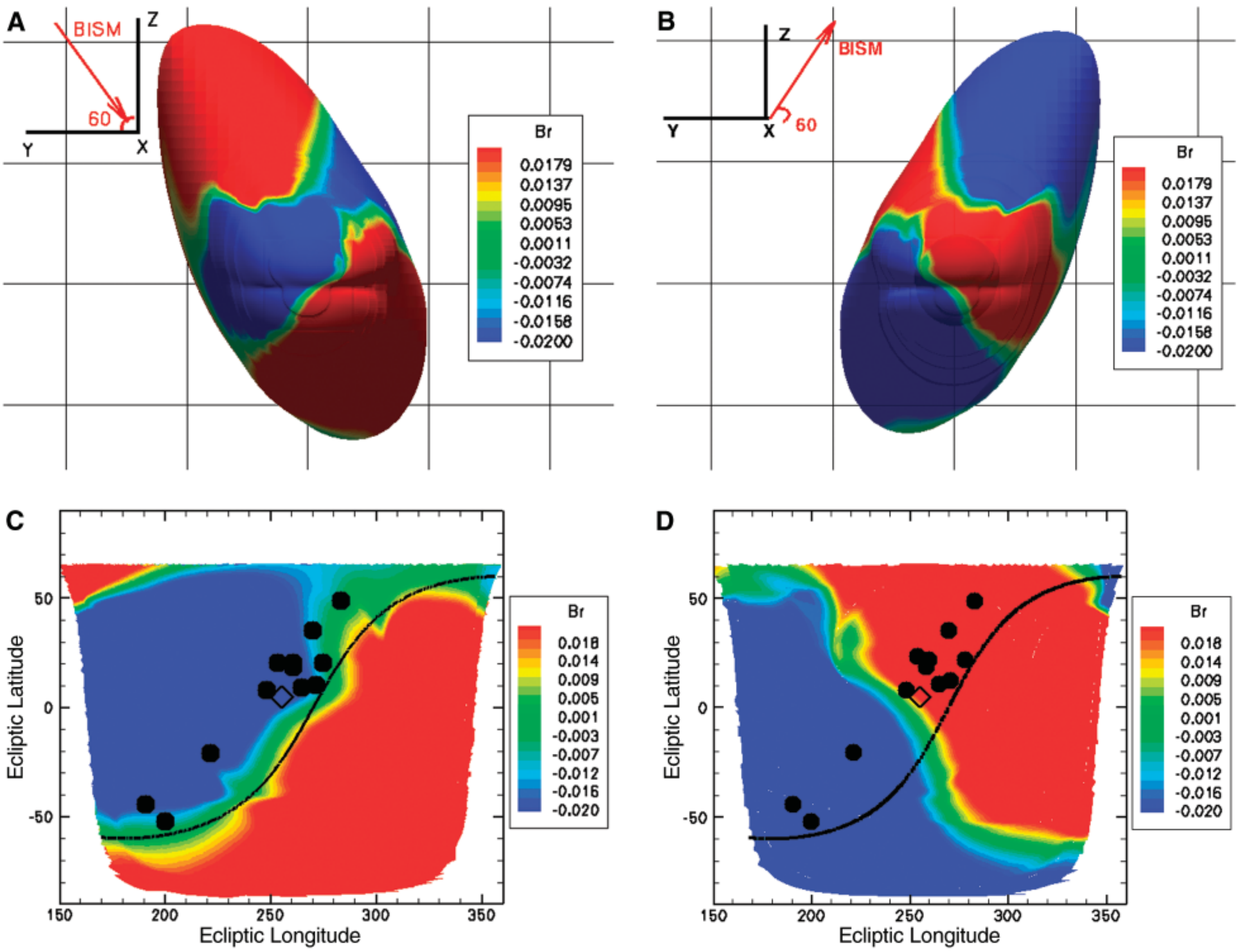

Fig. 1. (**A** and **B**) Radio source location as a function of the interstellar magnetic field (B_{ISM}) direction in (A) the HDP plane and (B) the GAL plane (with $\alpha = 45°$). The surface of the heliopause is shown from upwind with respect to the interstellar wind. The isocontours show the strength of the radial component of the interstellar magnetic field, B_r, on the heliopause. The green band is the location of the radio sources (at $B_r = 0$). The red arrows show the direction of B_{ISM}. (**C** and **D**) Same as (A) and (B) but converted to ecliptic coordinates for B_{ISM} in (C) the PPG (with $\alpha = 30°$) and (D) the GAL (with $\alpha = 45°$). The direction of the nose of the heliosphere (diamond) and the GAL (black line) are indicated for reference. The radio sources detected by V1 and V2 are shown as solid circles. Note that the colors are inverted from (C) to (D) because the interstellar magnetic direction was inverted from (A) to (B) (see red vectors in the insets).

the tangential field condition for the radio sources translates to $B_r = 0$, where B_r is the radial component of the interstellar magnetic field. For each modeled direction of the interstellar magnetic field, we compared the expected location of the radio sources ($B_r = 0$ at the heliopause) with the observed location of the radio sources detected by V1 and V2.

The model used here is the same as used by (*3*) [see (*12*)]. The interstellar magnetic field (B_{ISM}) magnitude is taken to be $B_{ISM} = 1.8$ μG [with the y component of B_{ISM} ($B_{ISM,y}$) < 0]. The coordinate system has the interstellar velocity direction in the $+x$ direction and the z axis as the solar rotation axis of the Sun, with y completing the right-handed coordinate system. In this coordinate system, V1 is at 29.1° latitude and 213.4° longitude and V2 is at –31.2° latitude and 178.4° longitude, which ignores the 7.25° tilt of the solar equator with respect to the ecliptic plane.

Figure 1 indicates that the heliopause is strongly influenced by the interstellar magnetic field direction; the heliopause is asymmetric both north-south and east-west and has a plane of symmetry approximately parallel to the plane of the local interstellar magnetic field. As a result, the heliopause surfaces for HDP and GAL field orientations are almost mirror images of each other.

With B_{ISM} parallel to the GAL (with α = 45°, Fig. 1D), the region where $B_r = 0$ is almost perpendicular to the GAL, which is inconsistent with the radio observations. With B_{ISM} in the PPG with α = 30° (Fig. 1C) produces the best agreement with the Voyager radio observations, as suggested by Gurnett *et al.* (*13*). The HDP orientation differs from that of PPG by only 16° and is also in general agreement, as suggested by the similarity of the regions with $B_r = 0$ in Fig. 1A (HDP) and Fig. 1C (PPG). The offset of ~15° between the observations and the region with $B_r = 0$ for the model in best agreement (Fig. 1C) indicates that the accuracy of the model is not adequate to distinguish between the PPG and HDP field orientations.

We also investigated the effects of changing the interstellar wind direction to 5° above the ecliptic plane [in the solar ecliptic coordinate system, the interstellar wind direction is 255° (longitude) and 5° (latitude)] and changing the intensity of B_{ISM} from 1.8 μG to 2.5 μG. For both cases, the change in the predicted location of radio sources was minor (*12*). As α increases from 15° to 60°, the $B_r = 0$ band moves counterclockwise, with the best agreement for α = 30° to 45° (*12*).

The second set of observational data that we used to constrain the orientation of the local interstellar magnetic field was the streaming ions from the termination shock. V1 crossed the termination shock at 94 AU in December 2004 and is now beyond 100 AU in the heliosheath (*1*, *2*, *14*). V2 is already detecting signs of the upcoming shock (*2*, *15*) and is expected to cross the termination shock within the next 1 to 2 years. In mid-2002, V1 began observing enhanced intensities of ions streaming from the shock (*16*, *17*). The beams of energetic termination shock particles (TSPs) were streaming outward along the solar spiral magnetic field. The strong upstream TSP beams were observed much of the time until V1 crossed the shock at 94 AU. The streaming along the magnetic field upstream of the shock source was expected to be inward along the spiral field if the termination shock were spherical. However, the observed flow was outward along the field, requiring a shock source located inward along the spiral field several AU closer to the Sun than is V1. With a nonspherical shock, V1 could be connected to the termination shock along magnetic field lines that crossed the termination shock and crossed back to the supersonic solar wind. This led to the suggestion that the upstream

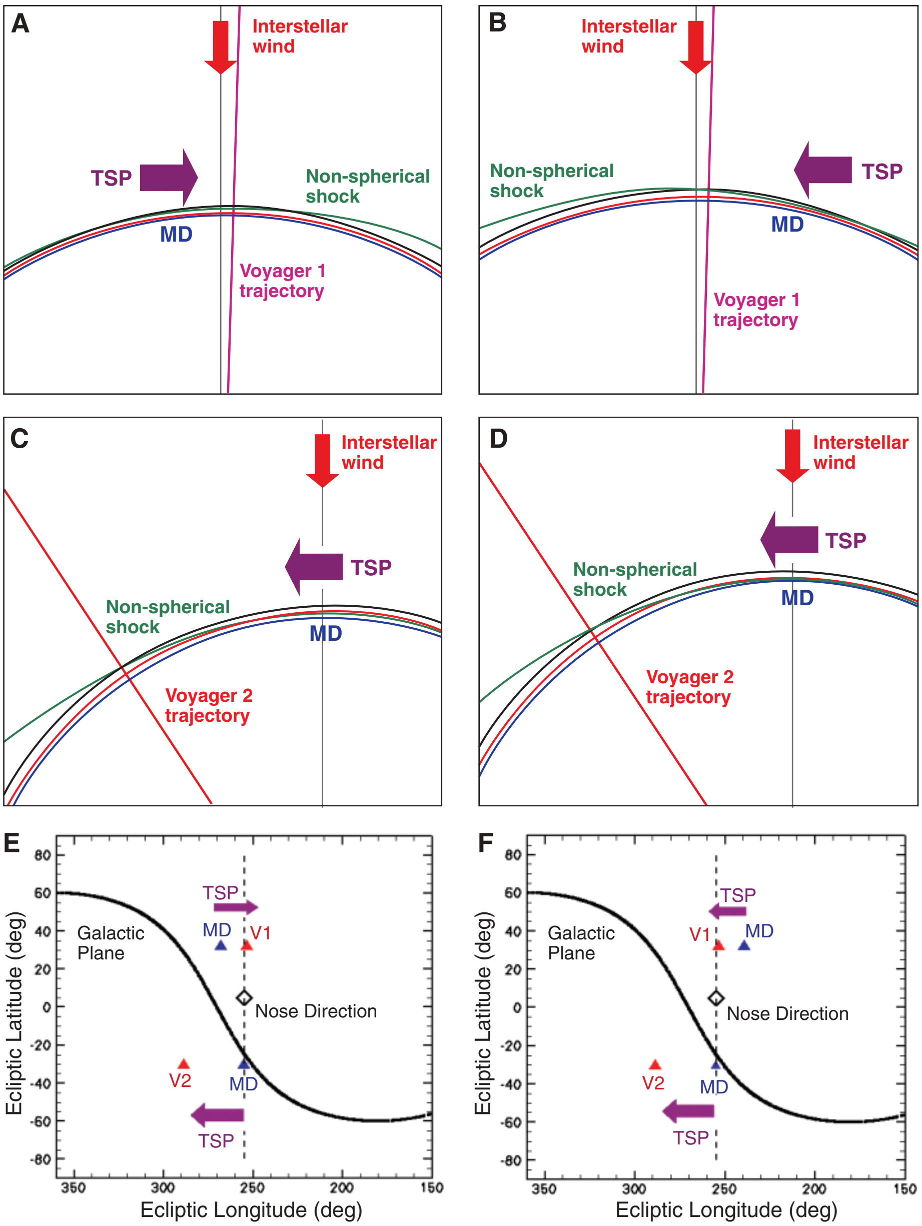

Fig. 2. (**A** and **B**) Streaming of TSPs from the MD point to V1 for the interstellar magnetic field in (A) the HDP (with α = 45°) and (B) the GAL (with α = 45°). The interplanetary magnetic field is carried radially outward by the solar wind, forming a spiral on a conical surface. The conical surfaces coinciding with the V1 trajectory are shown. V1 is first connected to the shock along the spiral magnetic field lines that contact the shock at the MD point. The solar magnetic field lines that intersect V1 are colored as follows: black, the 0 AU field line intersecting the shock where V1 crosses the shock; red and blue, magnetic field lines 2.0 AU and 3.0 AU upwind, respectively, from the 0 AU line; green, the nonspherical termination shock. The magenta arrow indicates the streaming direction of the TSPs from the shock along the field line to V1. (**C** and **D**) Similar plots for V2, showing field lines 3.0 AU (red) and 5.0 AU (blue) upwind of the 0 AU line. Note that in both views the solar magnetic field spirals clockwise with increasing distance outward. (**E** and **F**) Summary of the streaming of TSPs from the MD point back to V1 and V2. The nose direction (diamond) and the GAL are indicated.

beaming resulted from a blunt (*18*) or asymmetric shock (*2*). The asymmetric shock could result from an interstellar magnetic field inclined in a particular direction (*19*, *20*). In a recent report (*3*), we showed that an interstellar magnetic field in the HDP could distort the termination shock in a direction that explains the TSPs streaming outward at V1.

Figure 2 shows that for B_{ISM} parallel to the HDP, the longitude of the MD point (the minimum radial distance of the termination shock to the Sun) is greater than the longitude of V1, so the TSPs will stream outward along the spiral field. In the heliospheric southern hemisphere the longitude of V2 is greater than that of the MD point of the shock, so the TSPs will stream inward toward V2, as is observed. However, for B_{ISM} parallel to the GAL, the MD in the northern hemisphere shifts to a smaller longitude than V1, so that the TSPs would stream inward toward V1, opposite to what is observed.

In this calculation we did not include the neutral hydrogen atoms that interact with the ionized component by charge exchange. Although the inclusion of the neutral atoms will tend to symmetrize the solution and quantitatively affect the degree of asymmetry, the general character of the asymmetry is expected to remain the same, with the plane of symmetry of the distorted heliopause determined by the plane of the local interstellar magnetic field (*21*, *22*). Thus, it would be expected that different orientations of the local interstellar magnetic field would result in the same qualitative differences in the predicted radio source locations and streaming directions of upstream ions as described here. On the basis of those differences, and assuming that the source of radio emission is the region where the field draped on the heliopause is perpendicular to the radial direction, we find from Voyager observations that the plane of the local interstellar magnetic field is not parallel to the GAL but is 60° to 90° from that plane (rotated clockwise from a view from the Sun). This suggests that the field orientation in the Local Interstellar Cloud differs from that of a larger-scale interstellar magnetic field thought to parallel the GAL.

References and Notes

1. R. B. Decker *et al.*, *Science* **309**, 2020 (2005).
2. E. C. Stone *et al.*, *Science* **309**, 2017 (2005).
3. M. Opher, E. C. Stone, P. C. Liewer, *Astrophys. J.* **640**, L71 (2006).
4. P. C. Frisch, in *Physics of the Outer Heliosphere: Proceedings of the 1st COSPAR Colloquium* (Pergamon, Oxford, UK, 1990), pp. 19–28.
5. P. C. Frisch, *Space Sci. Rev.* **78**, 213 (1996).
6. R. Lallement *et al.*, *Science* **307**, 1447 (2005).
7. W. S. Kurth, D. A. Gurnett, F. L. Scarf, R. L. Poynter, *Nature* **312**, 27 (1984).
8. D. A. Gurnett, W. S. Kurth, S. C. Allendorf, R. L. Poynter, *Science* **262**, 199 (1993).
9. D. A. Gurnett, W. S. Kurth, E. C. Stone, *Geophys. Res. Lett.* **30**, 10.1029/2003GL018514 (2003).
10. D. A. Gurnett, W. S. Kurth, *Adv. Space Sci.* **16**, 279 (1995).
11. W. S. Kurth, D. A. Gurnett, *J. Geophys. Res.* **108**, 10.1029/2003JA009860 (2003).
12. See supporting material on *Science* Online.
13. D. A. Gurnett, W. S. Kurth, I. H. Cairns, J. Mitchell, *AIP Conf. Proc.* **858**, 129 (2006).
14. L. F. Burlaga *et al.*, *Science* **309**, 2027 (2005).
15. A. C. Cummings *et al.*, American Geophysical Union, Fall Meeting 2005, abstract SH51A-1184 (2005).
16. F. B. McDonald *et al.*, *Nature* **426**, 48 (2003).
17. S. M. Krimigis *et al.*, *Nature* **426**, 45 (2003).
18. J. R. Jokipii, J. Giacalone, J. Kota, *Astrophys. J.* **611**, L141 (2004).
19. R. Ratkiewicz *et al.*, *Astron. Astrophys.* **335**, 363 (1998).
20. N. V. Pogorelov, T. Matsuda, *J. Geophys. Res.* **103**, 237 (1998).
21. N. V. Pogorelov, G. P. Zank, *Astrophys. J.* **636**, L161 (2006).
22. V. Izmodenov, D. Alexashov, A. Myasnikov, *Astron. Astrophys.* **437**, L35 (2005).
23. We thank the staff at NASA Ames Research Center for the use of the Columbia supercomputer.

Supporting Online Material
www.sciencemag.org/cgi/content/full/316/5826/875/DC1
SOM Text
Figs. S1 to S4
References

3 January 2007; accepted 27 March 2007
10.1126/science.1139480

Ultralow Friction of Carbonate Faults Caused by Thermal Decomposition

Raehee Han,[1]* Toshihiko Shimamoto,[2]† Takehiro Hirose,[2]‡ Jin-Han Ree,[1] Jun-ichi Ando[3]

High-velocity weakening of faults may drive fault motion during large earthquakes. Experiments on simulated faults in Carrara marble at slip rates up to 1.3 meters per second demonstrate that thermal decomposition of calcite due to frictional heating induces pronounced fault weakening with steady-state friction coefficients as low as 0.06. Decomposition produces particles of tens of nanometers in size, and the ultralow friction appears to be associated with the flash heating on an ultrafine decomposition product. Thus, thermal decomposition may be an important process for the dynamic weakening of faults.

The strength of seismogenic faults, which is frictional resistance to fault slip during earthquakes, has been a major subject of debate in fault mechanics for 30 years (*1*, *2*). Although the stress–heat flow paradox for the San Andreas fault (no heat-flow anomaly, contrary to the prediction from in situ stress measurement and laboratory data of rock friction) favors extremely low fault strength (*3*, *4*), reasons for the weakness have been unclear. Recent work has shown that the dynamic weakening of faults during seismic slip can be caused by mechanisms such as frictional melting (*5*–*9*), thermal pressurization (*10*–*13*), and silica-gel formation (*14*, *15*). Fault gouge was also shown to exhibit pronounced slip weakening at high slip rates (*16*), presumably because of flash heating (*13*). Some analyses have predicted that slip-weakening distance, over which the initial peak friction drops to steady-state dynamic friction (*8*, *12*), and fracture energy (*13*, *16*) are of the same order as those parameters that are determined seismologically, narrowing the gap between laboratory studies of fault mechanics and seismology. Modeling the generation of large earthquakes is now becoming possible on the basis of the measured mechanical and transport properties of fault zones. Moreover, the dynamic weakening of faults may explain the lack of heat-flow anomaly after earthquake events along the San Andreas fault.

Thermal decomposition of rock-forming minerals at high ambient temperature and pressure can dramatically lower the strength of rocks because of the buildup of pore fluid pressure and the associated reduction of effective normal stress, provided that the sample is effectively undrained (*17*). Even at shallow crustal levels with low ambient temperature, thermal decomposition may occur at an elevated temperature because of coseismic frictional heating along fault zones. We demonstrated that a carbonate fault can lose frictional strength almost completely because of the thermal decomposition of calcite caused by frictional heating during high-velocity friction experiments on Carrara marble at seismic slip rates.

Forty-two friction experiments were conducted on precut bare surfaces of a pair of solid cylindrical specimens of Carrara marble (~99% calcite) at room temperature and room humidity. The experiments were carried out at normal stresses of 1.1 to 13.4 MPa and at equivalent slip rates of 0.03 to 1.30 m s^{-1}, with a rotary-shear, high-velocity friction apparatus at Kyoto University (*18*). The diameter and length of the specimen were 21.8 to 24.8 mm and about 20 mm, respectively (*19*). Because there is a slip-rate gradient across the fault due to cylindrical specimen geometry, we use the term "equivalent slip rate" ("slip rate" or "velocity" hereafter) (*7*, *18*, *19*).

[1]Department of Earth and Environmental Sciences, Korea University, Seoul 136-701, South Korea. [2]Division of Earth and Planetary Sciences, Graduate School of Science, Kyoto University, Kyoto 606-8502, Japan. [3]Department of Earth and Planetary Systems Science, Hiroshima University, Higashi-Hiroshima 739-8526, Japan.

*To whom correspondence should be addressed. E-mail: rhhan@korea.ac.kr

†Present address: Department of Earth and Planetary Systems Science, Hiroshima University, Higashi-Hiroshima 734-8526, Japan.

‡Present address: Instituto Nazionale di Geofisica e Vulcanologia, 00143 Rome, Italy.